

pubs.acs.org/cm Article

### Thermoelectric Oxide Ceramics Outperforming Single Crystals Enabled by Dopant Segregations

Cesar-Octavio Romo-De-La-Cruz, Yun Chen, Liang Liang, Mark Williams, and Xueyan Song\*



Cite This: Chem. Mater. 2020, 32, 9730-9739



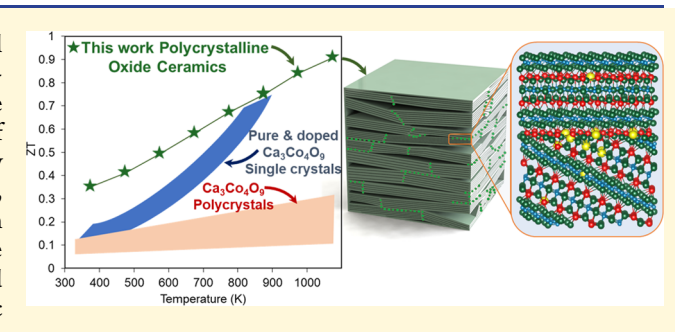
**ACCESS** 

III Metrics & More

Article Recommendations

3 Supporting Information

ABSTRACT: Calcium cobaltite  $Ca_3Co_4O_{9+\delta}$  in a single-crystal form was reported with an extrapolated dimensionless thermoelectric figure of merit of 0.87 in the year 2003. Regardless of the intensive effort during the past 2 decades, the performance of polycrystalline ceramics remained low and was reported to be only ~30 to 60% of that found for single crystals. Here, for the first time, the designed nonstoichiometric  $Ca_{3-x}Tb_xCo_4O_{9+\delta}Bi_y$  ceramics with intragranular dopant substitution are introduced, where the undersized dopant of Tb depletes at the grain boundaries and the oversized Bi segregates at the grain boundaries. Such synergetic dopant distribution simultaneously increases the electrical con-



ductivity and the Seebeck coefficient and results in the oxide ceramics with a peak ZT of 0.9, outperforming single crystals over a wide range of temperatures.

#### 1. INTRODUCTION

Thermoelectric (TE) technology<sup>1-4</sup> could be much more efficient if the high-performance TE materials were made of nontoxic and earth-abundant elements and could perform in air directly up to high temperatures over 800 K, where highgrade waste heat is emitted from the manufacturing and power generation systems such as gas turbines and high-temperature fuel cells. The energy conversion efficiency of TE materials is governed by the dimensionless figure of merit, 5 ZT. ZT is defined as  $S^2 \sigma T / \kappa$ , where S is the Seebeck coefficient,  $\sigma$  is the electrical conductivity,  $S^2\sigma$  is the electrical power factor,  $\kappa$  is the thermal conductivity, and T is the absolute temperature. The high-performance ZT materials need to possess high electrical conductivity, high Seebeck coefficient, and low thermal conductivity. The efficiency reaches about 10% when ZT = 1, which is generally accepted as a criterion for practical applications. The well-developed TE materials eported since the 1990s are usually heavy, toxic, and low in abundance as natural resources. Furthermore, their thermal or chemical stability is inferior 10,11 and they only function in a strict oxygen-free environment at high temperatures. On the other hand, oxide ceramics are usually not regarded as proper candidates for TE applications because they have ionic bonding with a narrow band when compared with covalent alloys. The carrier concentrations and mobility in the oxides are usually 2 or 3 orders of magnitude lower than those in covalent materials and lead to low electrical conductivities. The interest in TE oxides emerged since the unexpected discovery of a large thermopower and Seebeck coefficient in Na<sub>v</sub>Co<sub>2</sub>O<sub>4</sub> in  $1997^{12}$  and in  $Ca_3Co_4O_{9+\delta}$  in  $2000.^{13}$  For  $Ca_3Co_4O_{9+\delta}^{7}$  unit cells with peculiar two-dimensional misfit layers and

incommensurate character, electrically conductive CoO<sub>2</sub> sheets have a strongly correlated electron system that serves as electronic transport layers, while electrically insulating rocksalt-type Ca<sub>2</sub>CoO<sub>3</sub> misfit layers serve as phonon scattering centers for reducing thermal conductivity. In the year 2003, an extrapolated ZT of 0.87 at 973 K14 in air was reported for Ca<sub>3</sub>Co<sub>4</sub>O<sub>9+δ</sub> single crystals, making Ca<sub>3</sub>Co<sub>4</sub>O<sub>9+δ</sub>, having low cost, lightweight, nontoxicity, and high thermal stability in air, at the cusp of being relevant for thermoelectric applications since then. 15-21 However, it is also due to the two-dimensional layered structure that Ca<sub>3</sub>Co<sub>4</sub>O<sub>9+\delta</sub> single crystals exhibit strong anisotropic electrical behavior. Electrical conductivity measured in the directions perpendicular and parallel to the a-bplane of the unit cell shows that the former is lower than the latter by a factor of 500-1000.<sup>22</sup> Thus, two-dimensional characteristics and grain boundaries become serious problems for the production of polycrystalline devices with high performance. The ZT of bulk polycrystalline ceramics with various dopants synthesized using different methods remained only 30-60% of that of the single crystals, as reported during the past 2 decades.<sup>22,23</sup>

Here, we show that the polycrystalline oxide with designed novel nonstoichiometry Ca<sub>2.95</sub>Tb<sub>0.05</sub>Co<sub>4</sub>O<sub>9+6</sub>Bi<sub>v</sub> exhibits a

Received: August 24, 2020 Revised: October 20, 2020 Published: November 6, 2020





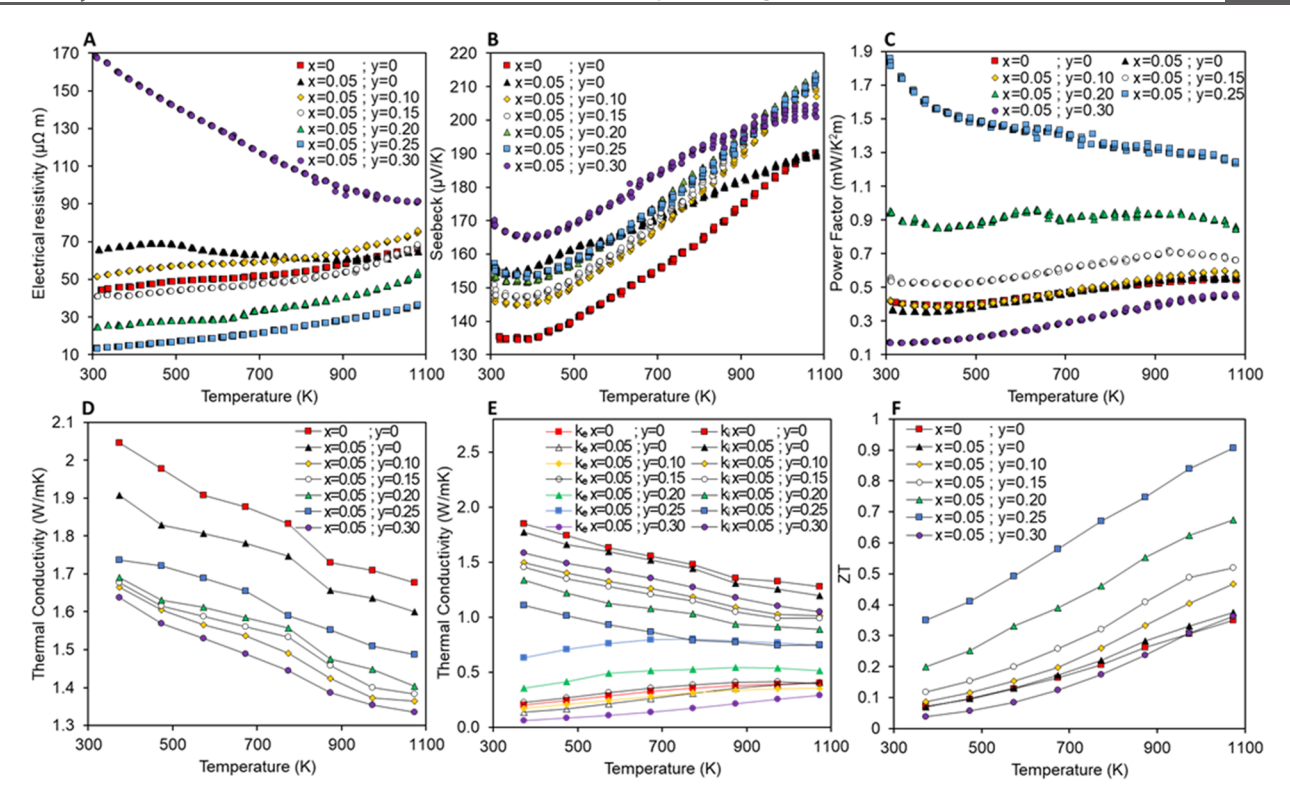


Figure 1. Temperature dependence of (A) electrical resistivity  $(\rho-T)$ , (B) Seebeck coefficient (S-T), (C) electrical power factor  $(S^2/\rho-T)$ , (D) total thermal conductivity  $(\kappa-T)$ , (E) electronic contribution  $(\kappa_{\rm e})$  and lattice contribution  $(\kappa_{\rm i})$ , and (F) thermoelectric figure of merit (ZT) for  ${\rm Ca}_{3-x}{\rm Tb}_x{\rm Co}_4{\rm O}_{9+\delta}{\rm Bi}_y$ .

tremendous increase (460% at 310 K and ~230% at 1073 K) in the electrical power factor compared to that of the pristine  $Ca_3Co_4O_{9+\delta}$  ceramics and reaches a peak ZT of 0.9 at 1073 K and average ZT of 0.63 from 373 to 1073 K, which is outperforming the single crystals over a wide range of temperatures. Such a leap in power factor and ZT was achieved through the concurrent introduction of unharmonized dual dopants of oversized Bi and undersized Tb. Whereas both Bi and Tb substitute host ions, the undersized dopant of Tb presents depletion at the grain boundaries and oversized Bi presents segregation at the grain boundaries. The carrier filtering performed by the dopant grain boundary segregation decreases the carrier concentration and increases the Seebeck coefficient. The lowered grain boundary energy, which also resulted from the dopant segregation, simultaneously enhances the crystal texture and increases the electrical conductivity. As such, the grain boundary with dopant segregation, regarded as the interface phase with a larger number of inequivalent atoms, has effectively decoupled the strongly correlated parameters of the Seebeck coefficient and electrical conductivity in the polycrystalline TE ceramics, resulting in a large increase in the electrical power factor. The present work sheds light on a new direction for engineering grain boundaries to dramatically improve the performance of various TE materials.

## 2. LARGE INCREASE IN THE ELECTRICAL POWER FACTOR AND *ZT*

The conventional chemical sol—gel method was used to synthesize precursor powders, which were subsequently subjected to calcination followed by cold pressing and sintering to formulate bulk scale pellets, as shown in Figure S1. Dopants were introduced at the sol—gel state to ensure the strict

chemistry and nonstoichiometry design in the final bulk ceramics. In the  $Ca_3Co_4O_{9+\delta}$  unit cell,  $Ca^{2+}$  and  $Co^{2+}/Co^{3+}$ have radii of 114 and 80 pm, respectively. Since the ionic radius sizes of Tb<sup>3+</sup>/Tb<sup>4+</sup> are 106 and 90 pm, respectively, and smaller than that of Ca<sup>2+</sup>, the heavy but the undersized Tb ion is first introduced as a dopant to scatter phonons and reduce the thermal conductivity. The small amount of doping at x =0.05 in  $Ca_{3-x}Tb_xCo_4O_{9+\delta}$  decreases the thermal conductivity to about ~92% of that of baseline. Meanwhile, the high oxidation state of rare-earth elements also alters the electrical carrier concentration, and a higher doping level results in an increase of both the electrical Seebeck coefficient and electrical resistivity, as shown in Figure 1. In  $Ca_{2.95}Tb_{0.05}Co_4O_{9+\delta}$ , there is a slight increase in the ZT up to 0.38 at 1073 K compared to the value of 0.35 for pristine  $Ca_3Co_4O_{9+\delta}$  as shown in Figures 1F and S2F. Upon this chemistry optimization of Tb concentration, Bi is further introduced to the Tb-doped Ca<sub>2.95</sub>Tb<sub>0.05</sub>Co<sub>4</sub>O<sub>9+δ</sub> ceramics. Bi is one of the first doping elements utilized to substitute Ca to introduce negative charge carriers and increase the Seebeck coefficient.<sup>24</sup> However, our previous work shows that the slightly oversized trivalent solute Bi<sup>3+</sup>, with an ionic radius of 117 pm, segregated at grain boundaries of the polycrystalline Ca<sub>3-x</sub>Bi<sub>x</sub>Co<sub>4</sub>O<sub>9+δ</sub> sample.<sup>25</sup> Such intergranular segregation apparently causes the intragranular chemistry to deviate from the designed stoichiometry. To compensate for the intragranular chemistry deviation, in the present work, Bi is introduced by nonstoichiometry addition with designed sample nominal chemistry of Ca<sub>2,95</sub>Tb<sub>0,05</sub>Co<sub>4</sub>O<sub>9+δ</sub> Bi<sub>v</sub>. For those ceramic pellets with high density (Table S1), Figure 1A shows a continuous decrease of electrical resistivity with an increase in the Bi addition level up to y = 0.25. At a lower-temperature regime, ceramics with dual dopants Bi and Tb present a similar S to that with unary

dopant Tb. However, at a temperature higher than 800 K, the samples with dual dopants present a much higher Seebeck coefficient than that with Tb doping alone. The sample with Bi doping level y=0.3 is overdoped with a large increase in electrical resistivity,  $\rho$ . Due to the low  $\rho$  and the enhanced S, the power factor continuously increases with Bi to y=0.25 for  $Ca_{2.95}Tb_{0.05}Co_4O_{9+\delta}Bi_{y_0}$  as shown in Figure 1C. It is worth noting that the power factor of  $Ca_{2.95}Tb_{0.05}Co_4O_{9+\delta}Bi_{0.25}$  at 310 K is 1.83 mW m<sup>-1</sup> K<sup>-2</sup>, which is 460% of that from baseline and also by far the highest power factor reported for  $Ca_3Co_4O_{9+\delta}$  synthesized with different methods and incorporation of different dopants. <sup>26</sup> At a high temperature of 1073 K, the sample with  $Ca_{2.95}Tb_{0.05}Co_4O_{9+\delta}Bi_{0.25}$  maintains an exceptionally high power factor of 1.23 mW m<sup>-1</sup> K<sup>-2</sup>, which is 230% of the baseline.

The Bi addition into the Tb-doped samples further impacts the thermal conductivity, revealing a complex trend with the Bi addition level. Figure 1D shows first a reduction of  $\kappa$  for y =0.10, then a gradual increase of  $\kappa$  with the increasing Bi doping level up to y = 0.25, and finally a reduction of the overall  $\kappa$  for the y = 0.3 doping level. The total  $\kappa$  is cumulative electronic thermal conductivity ( $\kappa_e$ ) and the lattice thermal conductivity  $(\kappa_i)$ , as depicted in Figure 1E. For Ca<sub>3</sub>Co<sub>4</sub>O<sub>9+ $\delta$ </sub> ceramics with  $\kappa_i$ being the predominant component contributing to the thermal conductivity, there is a continuous decrease in the  $\kappa_i$  with the increasing Bi doping level up to y = 0.25. Meanwhile, improvements in the electronic transport properties lead to an increase in the  $\kappa_e$  with the addition of Bi up to y = 0.25. The contribution of  $\kappa_e$  and  $\kappa_i$  thus resulted in a complex trend of total thermal conductivity upon Bi addition. Eventually, the sample Ca<sub>2.95</sub>Tb<sub>0.05</sub>Co<sub>4</sub>O<sub>9+δ</sub>Bi<sub>0.25</sub> with a high power factor is also with a slightly lower thermal conductivity than that of  $Ca_{2.95}Tb_{0.05}Co_4O_{9+\delta}$ . Overall, the  $Ca_{2.95}Tb_{0.05}Co_4O_{9+\delta}Bi_{0.25}$ ceramic has a remarkable peak ZT of 0.91 at 1073 K. Furthermore, largely due to the high electrical power factor at the low-temperature regime, the ZT is having a high plateau of 0.35-0.9 with an average ZT of 0.63 from 373 to 1073 K, as shown in Figure 1F. In comparison with the pristine  $Ca_3Co_4O_{9+\delta}$  with a peak ZT of ~0.35, the peak ZT is 0.9 in  $Ca_{2.95}Tb_{0.05}Co_4O_{9+\delta}Bi_{0.25}$  being enhanced by ~260%. This is mainly achieved by increasing the electrical power factor, while the thermal conductivity is decreased by only ~10%. This approach is very different from those used for increasing the ZT of conventional semiconductors. For conventional thermoelectric materials, to date, the observed dramatic ZT enhancements in various bulk nanostructured materials have merely come from the very large reductions in lattice thermal conductivity<sup>27,28</sup> rather than from improvement in power factors.29

### 3. SINGLE PHASE WITH IMPROVED CRYSTAL ALIGNMENT UPON DOPING

The characteristic X-ray powder diffraction (XRD) peaks from the  $Ca_3Co_4O_{9+\delta}$  phase with monoclinic symmetry were identified for  $Ca_{2.95}Tb_{0.05}Co_4O_{9+\delta}Bi_y$  samples (Figure S3). Different from the baseline  $Ca_3Co_4O_{9+\delta}$  that also presents a minor amount of  $Co_3O_4$ , no impurity phase is observed in the samples of  $Ca_{2.95}Tb_{0.05}Co_4O_{9+\delta}Bi_y$  with the Bi concentration up to y=0.25. The presence of the single phase in the present samples with Bi nonstoichiometric addition is fully consistent with the previous reports indicating that the cobaltite should be actually considered as a nonstoichiometric phase with respect to both the variable oxygen content and the Ca/Co

ratio.<sup>30</sup> The overdoped Ca<sub>2.95</sub>Tb<sub>0.05</sub>Co<sub>4</sub>O<sub>9+δ</sub>Bi<sub>0.30</sub> samples show a minor amount of both Co<sub>3</sub>O<sub>4</sub> and Ca<sub>3</sub>Co<sub>2</sub>O<sub>6</sub><sup>31</sup> secondary phases. The calculated lattice parameters are listed in Table S2. With the increase of the Bi doping level up to y = 0.25, there is an increase in a,  $b_1$ , c, and  $\beta$ , which is accompanied by a decrease in the lattice parameter  $b_2$ . Bi addition also triggers major microstructure changes. For Ca<sub>2.95</sub>Tb<sub>0.05</sub>Co<sub>4</sub>O<sub>9+δ</sub>Bi<sub>ν</sub> having elongated plate-shaped grains with large anisotropy, the longer dimension parallel to the a-b plane of the crystals gradually increases with Bi addition up to y = 0.25, while the dimension along the c-axes remained almost constant as shown in Figure S4. The crystal grain anisotropy is thus increased, implying the faster grain growth and faster diffusion along the a-b plane during the sintering. Such an increase in grain anisotropy is accompanied by the improvement of the crystal texture. For Ca<sub>2.95</sub>Tb<sub>0.05</sub>Co<sub>4</sub>O<sub>9+δ</sub>Bi<sub>0.25</sub> samples, the crystals have the c-axis of the monoclinic structure more or less parallel to the pressed direction of the pellets, although the misorientation angle  $\sim 30^{\circ}$  between the neighboring grains is commonly observed. The magnitude of the crystal texture was calculated with a Lotgering factor<sup>32</sup> of 0.959 for  $Ca_{2.95}Tb_{0.05}Co_4O_{9+\delta}Bi_{0.25}$  samples in comparison with that of 0.678 from a pristine sample. With the increase in the Bi doping level to y = 0.3, there is an abnormal large grain growth with random orientation.

## 4. INTRAGRANULAR DOPANT SUBSTITUTION AND INTERGRANULAR DOPANT DEPLETION AND SEGREGATION AT THE GRAIN BOUNDARY PLANES

Transmission electron microscopy (TEM) diffraction contrast images depict that each of the micron-sized crystal grains shown in the scanning electron microscopy (SEM) images is conformed by a conglomeration of nanolamellas having the same c-axes. The Z-contrast images from the samples with unary single dopant Tb, unary single dopant Bi, and dual dopants are shown in the columns of Figure 2A-C, respectively. Due to the big atomic number difference, the occupation of Tb or Bi in the Ca or Co sites of the Ca<sub>3</sub>Co<sub>4</sub>O<sub>9+δ</sub> lattice could be readily resolvable in the atomic resolution Zcontrast imaging. In the  $Ca_{2.95}Tb_{0.05}Co_4O_{9+\delta}$  sample in Figure 5A, the atomic columns with brighter intensity, presumably due to the Tb substitution, are only observed in the CaO atom layer. This is fully consistent with the designed chemistry of Tb substitution of Ca. By contrast, in  $Ca_3Co_4O_{9+\delta}Bi_{0.25}$ , the bright intensity is present in both the CaO layer and the CoO<sub>2</sub> layer, implying Bi substitution in both the Ca and Co sites of the  $Ca_3Co_4O_{9+\delta}$  lattice. For the  $Ca_{2.95}Tb_{0.05}Co_4O_{9+\delta}Bi_{0.25}$  sample with dual dopants, the bright atom columns are observed in both the CaO layer and the CoO<sub>2</sub> layer probably due to Tb occupation in the Ca sites and Bi present in both the Ca and Co sites. Both Tb and Bi exhibit random intragranular distribution in the  $Ca_3Co_4O_{9+\delta}$  lattice.

Consistent with XRD results revealing the single phase and consistent with STEM imaging revealing the Tb substitution of Ca and nonstoichiometric added Bi substitution of both Ca and Co, for all three samples, there is no secondary phase induced by either dopant at the grain boundaries (GB). Under TEM, energy-dispersive spectroscopy (EDS) was recorded on the grain boundaries and grain interior, as shown in Figure S5. For  $Ca_{2.95}Tb_{0.05}Co_4O_{9+\delta r}$  there is a presence of Tb in both the crystal lattice and the GBs with notably Tb depletion in the

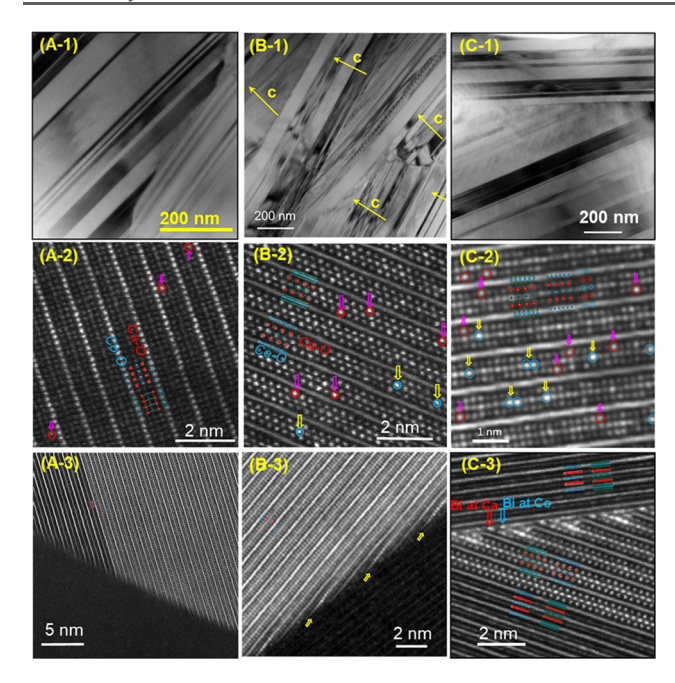


**Figure 2.** TEM and STEM images showing the nanostructure of  $Ca_{3-x}Tb_xCo_4O_{9+\delta}Bi_y$  samples. (A- ), (B- ), and(C- ) show the nanostructure of the lattice and grain boundary for  $Ca_{2.95}Tb_{0.05}Co_4O_{9+\delta}$ ,  $Ca_3Co_4O_{9+\delta}Bi_{0.25}$ , and  $Ca_{2.95}Tb_{0.05}Co_4O_{9+\delta}Bi_{0.25}$ , respectively. In (A-2), the arrows show the position of Tb in the rock salt layer CaO inside the lattice. In (B-2, B-3), the purple arrows show the position of Bi in the rock salt layer CaO inside the lattice, whereas the yellow arrows show the position of Bi in the rock salt layer CaO in both the lattice and the grain boundary. In (C-2, C-3), the purple arrows show the position of dopants in the rock salt layer CaO in both the lattice and the grain boundary, whereas the yellow arrows show the position of the dopants in the rock salt layer CaO in both the lattice and the grain boundary.

GBs. In  $Ca_{2.95}Tb_{0.05}Co_4O_{9+\delta}Bi_{0.25}$ , Bi is present at both the grain interior and the grain boundaries while Bi segregation at the GBs is accompanied by a slight Tb depletion.

The atomic structure of the grain boundaries is further revealed by atomic resolution Z-contrast imaging. Consistent with the TEM EDS results, the  $Ca_{2.95}Tb_{0.05}Co_4O_{9+\delta}$  sample (Figure 2A) did not present any brighter column at the grain boundaries, indicating the lack of the heavy element Tb at the grain boundaries. Interestingly, the grain boundaries of the Ca<sub>3</sub>Co<sub>4</sub>O<sub>9+δ</sub>Bi<sub>0.25</sub> sample present the bright column exclusively and periodically on the Co sites within the rock-salt-type Ca2CoO3 layers. Such brighter atom columns are initiated at the GB plane and extend about 3-4 atomic spacing into the grain interior. Such brighter contrast indicates the Bi segregation at the Co sites at the grain boundaries of the  $Ca_3Co_4O_{9+\delta}Bi_{0.25}$  sample. By contrast, in Ca<sub>2.95</sub>Tb<sub>0.05</sub>Co<sub>4</sub>O<sub>9+ô</sub>Bi<sub>0.25</sub>, there are brighter atomic columns on both the Ca and Co sites of the grain boundary planes. While the segregations are normally 1-2 atomic spacing onto the Ca sites, the Bi segregation on the Co sites is extensive, extending about 3-5 atoms on Co sites of the rock-salt-type Ca<sub>2</sub>CoO<sub>3</sub> misfit layers, indicating the intensified Bi segregation induced by dual dopants, probably caused by the Tb depletion at the grain boundary planes. To further understand the dopant concentration, the simulation was performed. As shown in Figure 3, for the atom columns with the strongest intensity, the maximum substitution occupancy of Bi on the Co sites is estimated to be ~29% (five Bi atoms in 17 possible atom sites

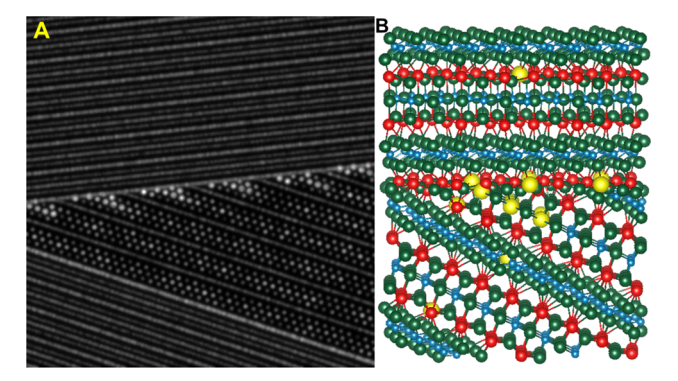


**Figure 3.** STEM images showing the nanostructure of  $Ca_{2.95}Tb_{0.05}Co_4O_{9+\delta}Bi_{0.25}$  for the simulated (A) results and the three-dimensional (3D) crystal structure (B).

in the simulation), whereas Bi occupancy is estimated to be lower,  $\sim$ 17% (three Bi atoms per 17 possible sites).

### 5. ATOMIC STRUCTURE ORIGIN OF THE INCREASED POWER FACTOR AND *ZT*

Although nonstoichiometric doping does not result in the secondary phase formation, the dual dopants have led to the systematic microstructure evolution, as schematized in Figure 4, including the increased grain anisotropy, improved crystal

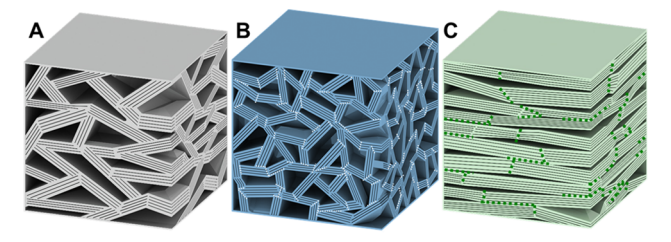


**Figure 4.** Schematic showing that the dual dopants have resulted in the systematic microstructure evolution: (A)  $Ca_3Co_4O_{9+\delta}$ . (B)  $Ca_{2.95}Tb_{0.05}Co_4O_{9+\delta}$ . (C)  $Ca_{2.95}Tb_{0.05}Co_4O_{9+\delta}$ Bi<sub>0.25</sub>.

grain alignment, and the segregation of dopants at the grain boundaries. Consistent with our previous results obtained by incorporating different sets of the oversized dopants K, 33 Ba, 3 and Bi,25 the present results indicate that the grain boundaries of the Ca<sub>3</sub>Co<sub>4</sub>O<sub>9+δ</sub> ceramics consistently attract oversized dopants while depleting the undersized dopants. The segregation of the oversized dopants decreases the grain boundary energy and facilitates fast diffusion along the grain boundaries and crystal alignment and crystal texture development. The improved crystal texture induced by dopant grain boundary segregation is fully consistent with what we have reported previously for the system with the appropriate level doping of single dopant Ba, 34 single dopant Bi, 25 and single dopant K.33 Such repeatable finding on the effect of the grain boundary segregation on the crystal texture development is also consistent with the literature reporting that grain boundary segregation decreases the grain boundary energy in ceramics, 35 and there is a strong inverse correlation between the relative energies of grain boundaries and the frequency with which they occur in microstructures and during microstructure evolution. 36-38 In other words, the relatively higher-energy grain boundaries are more likely to be shrinking, while lower-energy interfaces are more likely to be growing that lead to a steady-state distribution of grain boundaries. In

our case, it is the development of strong texture along the *c*-axis. The dopant grain boundary segregation and crystal alignment have profoundly decreased the electrical resistivity.

Interestingly, the introduction of oversized dopants also simultaneously increased the Seebeck coefficient. In the present study with dual dopants, the cause of the increased Seebeck coefficient could be multifold. First, Bi was intentionally added to the Tb-doped sample with designed nonstoichiometry to possibly compensate the Bi segregation at the grain boundaries. However, the amount of Bi could be continuously added to the  $Ca_3Co_4O_{9+\delta}$  grains without forming the secondary phase, which is surprising. As revealed by the Zcontrast imaging in Figure 2, in addition to the replacement of Ca, Bi also substitutes for Co, like those from the  $Bi_{*}Co_{2-x}MnO_{4}$  oxide.  $^{39}$  In the  $Ca_{3}Co_{4}O_{9+\delta}$  unit cell, each of the individual layers is contributing effectively in electrical and thermal transport. For  $Ca_{2.95}Tb_{0.05}Co_4O_{9+\delta}Bi_{0.25}$ , in the CaO layer, Bi<sup>3+</sup> incorporation decreases the carrier concentration. Meanwhile, in the CoO<sub>2</sub> layer, Bi<sup>3+</sup> with a larger ionic radius inevitably increases the abundance of Co<sup>4+</sup> ions with a smaller ionic radius than that of Co<sup>3+</sup> ions. The intragranular Seebeck coefficient thus increased accordingly.

Second, the increased Seebeck coefficient was also attributed to the dopant grain boundary segregation. The segregated dopants reside on the original sites of both Co and Ca, and the grain boundary plane with about four atomic spacing extends into the grain interior. As such, the grain boundary plane needs to be treated as a different crystalline phase with a larger number of nonequivalent atoms that could favor the high power factor as predicted by a high-throughput material design.<sup>40</sup> Owing to the abrupt structural asymmetry and chemical inhomogeneity in the localized volume, the grain boundaries also may exhibit novel functional properties that cannot be realized in bulk crystals. For example, the dopant cation segregation at oxide grain boundaries could inevitably result in the formation of the space-charge layer adjacent to the grain boundary plane, lead to the redistribution of charges and oxygen vacancies in the grain interiors, 27,41 and overwhelmingly affect the Seebeck coefficient. In principle, during the transport procedure, the carriers with energy higher than the Fermi energy contribute positively to the Seebeck coefficient, while the carriers with energy lower than the Fermi energy contribute negatively. The segregation of Bi at the GBs and the related space-charge layer acts as an obstructive layer to block the carrier transport through adjacent crystals, which also works to filter the carrier with low energy. 42 In other words, upon segregation, carrier propagation across the grain boundary only involves carriers with high energy, thus contributing to reducing the carrier concentration and increasing the Seebeck coefficient. Such decreased carrier concentration will apparently decrease the electrical conductivity  $\sigma$  in a way that satisfies  $\sigma = ne\mu$ , where  $\mu$  is the carrier mobility, e is the elementary positive charge constant, and n is the number density of electrons. Nevertheless, the measured continuous increase in electrical conductivity with Bi, shown in Figure 2A, is evidencing the dramatically increased carrier mobility  $\mu$  in Ca<sub>2.95</sub>Tb<sub>0.05</sub>Co<sub>4</sub>O<sub>9+ $\delta$ </sub>Bi<sub>0.25</sub> presumably due to the improved alignment of anisotropic crystal grains.

## 6. OXIDE CERAMICS OUTPERFORMING THE SINGLE CRYSTALS

The peak ZT of 0. 9 is the highest ZT value reported for  $Ca_3Co_4O_{9+\delta}$  oxide ceramics during the past 2 decades, as

shown in Table S3 and Figure 5. The  $Ca_{2.95}Tb_{0.05}Co_4O_{9+\delta}Bi_{0.25}$  sample also outperformed the single-crystal  $Ca_3Co_4O_{9+\delta}^{-14}$  and

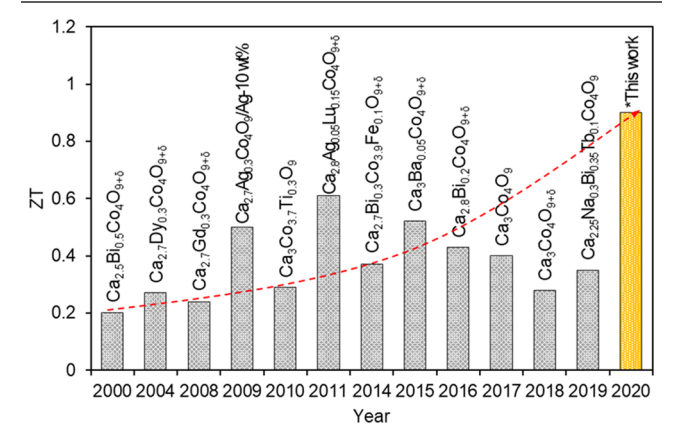


**Figure 5.** Timeline of the improvement in the ZT of  $\operatorname{Ca_3Co_4O_{9+\delta}}$  polycrystalline materials by the addition of different doping elements.  $^{13,25,34,51,59-89}$  \*The ZT value of this work is also reported. The goal of reaching a ZT material over 1 for commercial applications would be achievable within a few years. Table  $\operatorname{S3}^{67-89}$  shows historical progression of the thermoelectric properties of  $\operatorname{Ca_3Co_4O_{9+\delta}}$ .

 $Ca_{2.9}Bi_{0.1}Co_4O_{9+\delta}{}^{24}$  single crystals, as shown in Figure 6. The  $Ca_{2.95}Tb_{0.05}Co_4O_{9+\delta}Bi_{0.25}~$  polycrystalline ceramics possess apparently lower thermal conductivity in comparison with that of the single crystals. It is most worth noting that the Ca<sub>2.95</sub>Tb<sub>0.05</sub>Co<sub>4</sub>O<sub>9+δ</sub>Bi<sub>0.25</sub> polycrystalline ceramics also possess a higher electrical power factor than that of the single crystals, especially at the low-temperature regime. Such power factors of  $Ca_{2.95}Tb_{0.05}Co_4O_{9+\delta}Bi_{0.25}$  polycrystalline ceramics have directly resulted from the higher electrical Seebeck coefficient and low resistivity. As clearly shown in both the SEM and TEM images, the Ca<sub>2.95</sub>Tb<sub>0.05</sub>Co<sub>4</sub>O<sub>9+δ</sub>Bi<sub>0.25</sub> polycrystalline ceramics possess a high abundance of grain boundaries with the misorientation angle of ~30°. The low resistivity in  $Ca_{2.95}Tb_{0.05}Co_4O_{9+\delta}Bi_{0.25}$ compared to that of the single crystals immediately reveals that, when incorporating dopant segregation, the grain boundaries with the misorientation angle of ~30° do not reduce the electrical conductivity. Such results allow a wider processing window in the production of polycrystalline oxide ceramics and are very encouraging for practical TE application.

# 7. SIGNIFICANCE OF RESOLVING AND CONTROLLING THE ATOMIC STRUCTURE OF DOPANT SEGREGATION AT THE GRAIN BOUNDARIES

For polycrystalline materials, the dopants and their segregation at grain boundaries have a profound impact on the properties of the material. The ability to spatially resolve the atoms in grain boundaries would greatly advance our understanding of the correlation between the structure and property in materials. Consequently, the effect of dopant grain boundary segregation has been extensively investigated in model material systems ranging from structure materials to superconductors such as Ni, Al<sub>2</sub>O<sub>3</sub>, MgO, MgO, and YBa<sub>2</sub>Cu<sub>3</sub>O<sub>7</sub>. However, the understanding of the impact of grain boundaries on both the electrical and thermal transport properties of most thermoelectric materials is currently very limited. The potential of further controlling dopants and the related grain boundary engineering is largely unexplored in any TE materials.

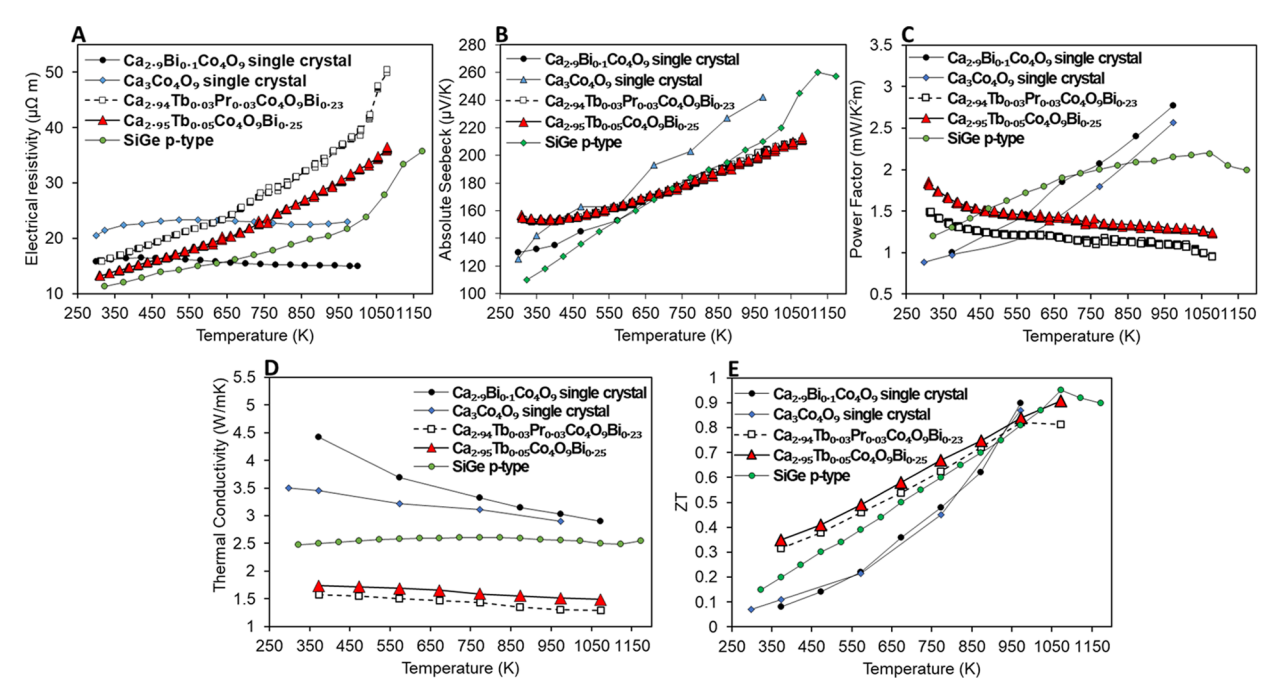


Figure 6. Temperature dependence of thermoelectric properties for different state-of-the-art p-type materials:  $^{14,24,52}$  (A)  $\rho$ -T, (B) S-T, (C)  $S^2/\rho$ -T, and (E) ZT.

Meanwhile, the realization of high ZT is very complicated because all of the three parameters Seebeck coefficient S, electrical conductivity  $\sigma_i$ , and thermal conductivity  $\kappa$  are functions of carrier density; they are interrelated and conflicting in the following two aspects: 47,48 (1) The Seebeck coefficient is inversely related to the carrier concentration  $n_i$ and electrical conductivity  $\sigma$  is related to the carrier concentration by  $\sigma = ne\mu$ , where  $\mu$  is the carrier mobility. Increasing the carrier concentration by doping to increase the electrical conductivity simultaneously reduces the Seebeck coefficient and results in a very limited increase in the overall power factor. (2) The electrical contribution  $\kappa_e$  to the thermal conductivity  $\kappa$  increases with carrier density. Decoupling of the electrical from thermal conductivity and decoupling of the electrical conductivity from the Seebeck coefficient have been thus pursued for decades since the 1990s, when the intense nanostructure engineering was employed for improving the performance of TE materials. 49,50

In line with nanostructure engineering such as introducing interfaces, the current approaches of tuning the dopants in the different sublayers and drive the dopants segregate to the grain boundaries may provide an alternative approach that is more effective for oxide ceramics subjected to high-temperature applications. In the present work, the intragranular Tb substitutes Ca, not the Co. On the other hand, Bi substitutes both Ca and Co. When dual dopants are employed, the CaO and  $\text{CoO}_x$  sublattices were tuned separately and simultaneously. Since the  $\text{CoO}_x$  and  $\text{Ca}_2\text{CoO}_3$  nanoblocks conduct the electrical and thermal transport separately, the dual dopants provide the means for tuning the electrical and thermal transport separately and simultaneously at the unit cell level.

Meanwhile, Tb presents depletion at the grain boundaries, while Bi segregates at the grain boundaries; the intragranular and intergranular dopants can also be tuned separately and simultaneously. In terms of the electrical properties, it is generally agreed that the electrical conductivity is heavily

affected by the grain boundaries, while the Seebeck coefficient is not affected by the grain boundary properties.<sup>51</sup> The above points are consistent with what we have concluded for the pristine  $Ca_3Co_4O_{9+\delta}$ . While the thermal conductivities and electrical conductivities both increase with the increase of the grain size, the Seebeck coefficient remains unchanged for the nondoped pristine samples with different grain sizes.<sup>51</sup> However, once dopant segregation remains sharply at the GB plane, without forming the amorphous or crystal secondary phase, it eliminates the excessive scattering of the carrier and avoids the increase in electrical resistivity. The grain boundary with dopant segregation should be regarded as the interface phase with a larger amount of unequal ions within a confined space, thus providing a barrier and filter for the low-energy carrier and thus further decreasing the carrier concentration and increasing the Seebeck coefficient. Meanwhile, the lowered grain boundary energy enhanced the crystal texture and increased the carrier mobility, resulting in higher electrical conductivity. As such, the dopant grain boundary segregation has effectively decoupled the strongly correlated parameters of the Seebeck coefficient and electrical conductivity in the polycrystalline TE ceramics.

## 8. OUTLOOK FOR FURTHER INCREASE OF THE THERMOELECTRIC PERFORMANCE AND THE IMMEDIATE IMPACT ON THERMOELECTRIC APPLICATIONS

As aforementioned, controlling dopant segregation presents a crucial step for decoupling the strongly correlated parameters and achieving a high ZT. In the present study, a high ZT from  $Ca_{2.95}Tb_{0.05}Co_4O_{9+\delta}Bi_y$  is achieved using only two dopants. The designed chemistry is further tunable in terms of dopant species and doping levels. As an example, by introducing the third element Pr and slightly lower the Bi doping level, the sample of  $Ca_{2.94}Pr_{0.03}Tb_{0.03}Co_4O_{9+\delta}Bi_{0.23}$  was synthesized and evaluated. The electrical power factor of  $Ca_{2.94}Pr_{0.03}Tb_{0.03}Co_4O_{9+\delta}Bi_{0.23}$  was slightly lower than that of

 $Ca_{2.95}Tb_{0.05}Co_4O_{9+\delta}Bi_{0.25}$ ; however, the thermal conductivity was also lowered due to the increased entropy. Eventually, the  $Ca_{2.94}Pr_{0.03}Tb_{0.03}Co_4O_{9+\delta}Bi_{0.23}$  sample is with a high ZT of 0.83 at 973 K. It is worth pointing out that the high performance of the present samples is achieved without the nonequilibrium nanostructure engineering processing. The dopant substitution and grain boundary segregation are achieved through high-temperature equilibrium sintering. Accordingly, such dopant segregation at the grain boundaries is expected to possess long-term thermodynamic stability upon an operation that is usually conducted at a temperature much lower than the sintering temperature.

Finally, it is worth mentioning that Ca<sub>2.95</sub>Tb<sub>0.05</sub>Co<sub>4</sub>O<sub>9+δ</sub>Bi<sub>025</sub> also outperformed the best reported p-type SiGe from 373 to 973 K.<sup>52</sup> In terms of energy conversion efficiency at the high temperature of over 800 K, the peak ZT of 0.9 at 1073 K may not be high enough to compete with the latest reported ZT of 2.2 achieved in PbTe-SrTe-based samples<sup>53</sup> and ZT of 2.3 achieved in GeTe-based samples.<sup>54</sup> However, the nontoxic oxide materials are having extremely low cost (only 5-10% of SiGe and BiTe);55 the materials are processed with the methods that are conventional and low cost and can be readily scaled up for massive production to allow the oxide to play a central role in the TE technology. As such, the peak ZT of 0.9 and the average ZT of 0.63 from 373 to 1073 K provide an allaround appealing figure for immediate applications in air up to 1233 K. Beyond niche market applications such as solid-state cooling and exposed type of high-sensitivity thermocouples, the oxide could enable numerous applications in power generation systems such as gas turbines, as well as other thermal energy recovery systems. Furthermore, the high chemical and thermal stability of the oxide allows for a larger temperature gradient applied across the oxide in air that leads to a higher energy conversion efficiency.

For the p-type  $Ca_{2.95}Tb_{0.05}Co_4O_{9+\delta}Bi_{0.25}$  developed in this study, when incorporating the doped n-type  $CaMnO_3^{57}$  with a high ZT of 0.64, uni-couple is expected to have a power density of 2.6 W cm<sup>-2</sup> when the temperature gradient is 700 K and the hot side temperature of 1073 K when operating in air. This power density is higher than the highest power density reported for a solid oxide when operating at 1023 K, even using  $H_2$  fuel. The TE generators could be incorporated into solid oxide fuel cell systems in air preheaters, steam generators, and exhaust outlets to further increase the overall energy conversion efficiency of the entire system.

#### 9. CONCLUSIONS

For the misfit-layered thermoelectric oxide, the present work demonstrates that dopant nonstoichiometric addition dramatically decoupled the strongly correlated parameters of the Seebeck coefficient and electrical conductivity and dramatically increased the electrical power factor by up to 460%, resulting in the polycrystalline oxide ceramics outperforming single crystals over a wide temperature range. The low-cost, nontoxic, and highly stable thermoelectric oxide ceramics with newly designed chemistry thus answer the quest of historic limitations of low efficiency and high cost of thermoelectric applications for decades. Meanwhile, for the first time, among all kinds of thermoelectric materials, the present work clearly resolved the atomic structure of grain boundaries with the solute segregation. Whereas the dopants segregating at the GBs promote the crystal texture and facilitate large carrier mobility and high electrical conductivity, the dopant GB segregation

will act as a carrier filter to decrease the carrier concentration and simultaneously increase the Seebeck coefficient. The present work sheds light on the new direction for engineering the atomic structure of grain boundaries to dramatically improve the performance of various TE materials.

#### 10. MATERIALS AND METHODS

The present work applied conventional cold pressing and sintering to make the oxide pellets using the powders synthesized through the chemical sol-gel route to precisely control the stoichiometry and dopant distribution with strict uniformity. The polycrystalline ceramic samples were prepared by the conventional chemical sol-gel route with chemical compositions  $Ca_{3-x}Tb_xCo_4O_{9+\delta}$  (x = 0, 0.05, 0.30, and0.50) and  $Ca_{2.95}Tb_{0.05}Co_4O_{9+\delta}Bi_v$  (y = 0.10, 0.15, 0.20, 0.25, and 0.30). The precursor powders were obtained by mixing chemical reagents: Ca(NO<sub>3</sub>)<sub>2</sub>·4H<sub>2</sub>O (99%, Acros Organics), Co(NO<sub>3</sub>)<sub>2</sub>·6H<sub>2</sub>O (99%, Acros Organics), Bi(NO<sub>3</sub>)<sub>3</sub>·5H<sub>2</sub>O (98%, Acros Organics), and Tb(NO<sub>3</sub>)<sub>3</sub>·6H<sub>2</sub>O (99.9% Strem Chemicals) in deionized water according to the stoichiometric chemical compositions. Citric acid (BDH Chemical), ethylene glycol, and poly(ethylene glycol) were dissolved in the solution to polymerize the mixture. Nitric acid was included in the solution to promote the sol-gel synthesis, nitrate salt decomposition, and the new compound formation. The sol-gel mixture was mechanically stirred at 353 K for 3 h. The obtained solgel mixture was ashed at 773 K for 2 h in the air inside a box furnace. The subsequent ashes were ball-milled in ethyl alcohol in a stage with zirconia balls and then dried at room temperature with a final manually ground stage to obtain uniform grain size in the powder. The reasonable homogeneous ashes were calcined at 973 K for 4 h in a tube furnace with constant oxygen flow. The calcined powders were uniaxially pressed into round pellets under a 1 GPa pressure at room temperature. The bulk samples were sintered at 1233 K in a tube furnace with constant oxygen flow and then cut into rectangular pellets to obtain the final desired sample for either the electrical or thermal measurements. The apparent densities for all bulk samples are listed in Table S1.

The electrical resistivity  $(\rho)$  and absolute Seebeck coefficient (S)were measured at the same time by the four-terminal method using a Linseis LSR-1100 unit. The measurements were performed perpendicular to the pressed direction from 323 to 1073 K under a low-pressure He environment. The thermal conductivity was calculated using the equation  $\kappa = \lambda C_p m$ , where  $C_p$ ,  $\lambda$ , and m are the specific heat, thermal diffusivity, and mass density, respectively. The  $\hat{C}_{_{D}}$  and  $\lambda$  values were obtained in the range 323–1073 K using Linseis Laser Flash Analyzer 1200. The measurements were also performed perpendicular to the pressed direction, and samples were analyzed under a low-pressure air environment. X-ray powder diffraction (XRD) analysis was performed using a PANatycal X'Pert Pro XRD unit for crystal phase and lattice parameter determination purposes. The ground powders from the sintered samples were used in the XRD analysis using Cu K $\alpha$  radiation, 45 kV voltage, and 40 mA current at room temperature. The cross-section and plan-view morphology of the sintered pellets was observed using a Hitachi-S4700F scanning electron microscope (SEM) unit. Transmission electron microscopy (TEM) samples were prepared from sintered pellets by mechanically polishing and ion milling in a liquid-nitrogen-cooled holder. TEM imaging including energy-dispersive spectroscopy (EDS) and highresolution TEM was performed using a JEM-2100 microscope operated at 200 kV. High-angle annular dark-field (HAADF) Zcontrast imaging and nanoscale chemistry analysis were performed using an aberration-corrected 200 kV (JEOL 2100F) STEM with the inner cut-off angle of the HAADF detector set at >52 mrad.

#### ASSOCIATED CONTENT

#### **5** Supporting Information

The Supporting Information is available free of charge at https://pubs.acs.org/doi/10.1021/acs.chemmater.0c03437.

Procedure of fabrication of polycrystalline ceramics pellets; temperature dependence of  $Ca_{3-x}Tb_xCo_4O_{9+\delta}$  samples; XRD powder diffraction patterns; SEM images of  $Ca_{3-x}Tb_xCo_4O_{9+\delta}Bi_y$  samples after the sintering stage; TEM images showing the nanostructure of the  $Ca_{2.95}Tb_{0.05}Co_4O_{9+\delta}Bi_y$  samples; apparent density of the  $Ca_{3-x}Tb_xCo_4O_{9+\delta}Bi_y$  samples; lattice parameters of the  $Ca_{3-x}Tb_xCo_4O_{9+\delta}Bi_y$  samples; and progression of the performance of  $Ca_3Co_4O_{9+\delta}$  (PDF)

#### AUTHOR INFORMATION

#### **Corresponding Author**

Xueyan Song — Department of Mechanical and Aerospace Engineering, West Virginia University, Morgantown, West Virginia 26506, United States; orcid.org/0000-0002-9878-5883; Email: xueyan.song@mail.wvu.edu

#### **Authors**

- Cesar-Octavio Romo-De-La-Cruz Department of Mechanical and Aerospace Engineering, West Virginia University, Morgantown, West Virginia 26506, United States; orcid.org/0000-0002-0170-2552
- Yun Chen Department of Mechanical and Aerospace Engineering, West Virginia University, Morgantown, West Virginia 26506, United States
- Liang Liang Department of Mechanical and Aerospace Engineering, West Virginia University, Morgantown, West Virginia 26506, United States
- Mark Williams Keylogic, Morgantown, West Virginia 26505, United States

Complete contact information is available at: https://pubs.acs.org/10.1021/acs.chemmater.0c03437

#### Notes

The authors declare no competing financial interest.

#### ACKNOWLEDGMENTS

C.-O. R.-D.-L.-C., L.L., and X.S. greatly acknowledge the support from NSF-DMR 1254594 and NSF-DMR 1916581.

#### REFERENCES

- (1) He, J.; Tritt, T. M. Advances in Thermoelectric Materials Research: Looking Back and Moving Forward. *Science* **2017**, 357, No. eaak9997.
- (2) Brown, S. R.; Kauzlarich, S. M.; Gascoin, F.; Snyder, G. J. Yb<sub>14</sub>MnSb<sub>11</sub>: New High Efficiency Thermoelectric Material for Power Generation. *Chem. Mater.* **2006**, *18*, 1873–1877.
- (3) Snyder, G. J.; Toberer, E. S. Complex Thermoelectric Materials. *Nat. Mater.* **2008**, *7*, 105–114.
- (4) Hinterleitner, B.; Knapp, I.; Poneder, M.; Shi, Y.; Müller, H.; Eguchi, G.; Eisenmenger-Sittner, C.; Stöger-Pollach, M.; Kakefuda, Y.; Kawamoto, N.; Guo, Q.; Baba, T.; Mori, T.; Ullah, S.; Chen, X.-Q.; Bauer, E. Thermoelectric Performance of a Metastable Thin-Film Heusler Alloy. *Nature* **2019**, *576*, 85–90.
- (5) Borup, K. A.; de Boor, J.; Wang, H.; Drymiotis, F.; Gascoin, F.; Shi, X.; Chen, L.; Fedorov, M. I.; Müller, E.; Iversen, B. B.; Snyder, G. J. Measuring Thermoelectric Transport Properties of Materials. *Energy Environ. Sci.* **2015**, *8*, 423–435.
- (6) Yan, J.; Gorai, P.; Ortiz, B.; Miller, S.; Barnett, S. A.; Mason, T.; Stevanović, V.; Toberer, E. S. Material Descriptors for Predicting Thermoelectric Performance. *Energy Environ. Sci.* **2015**, *8*, 983–994.
- (7) Alberi, K.; Nardelli, M. B.; Zakutayev, A.; Mitas, L.; Curtarolo, S.; Jain, A.; Fornari, M.; Marzari, N.; Takeuchi, I.; Green, M. L.; Kanatzidis, M.; Toney, M. F.; Butenko, S.; Meredig, B.; Lany, S.;

- Kattner, U.; Davydov, A.; Toberer, E. S.; Stevanovic, V.; Walsh, A.; Park, N.-G.; Aspuru-Guzik, A.; Tabor, D. P.; Nelson, J.; Murphy, J.; Setlur, A.; Gregoire, J.; Li, H.; Xiao, R.; Ludwig, A.; Martin, L. W.; Rappe, A. M.; Wei, S.-H.; Perkins, J. The 2019 Materials by Design Roadmap. *J. Phys. D: Appl. Phys.* 2018, *52*, No. 013001.
- (8) Ying, P.; Li, X.; Wang, Y.; Yang, J.; Fu, C.; Zhang, W.; Zhao, X.; Zhu, T. Hierarchical Chemical Bonds Contributing to the Intrinsically Low Thermal Conductivity in  $\alpha$ -MgAgSb Thermoelectric Materials. *Adv. Funct. Mater.* **2017**, 27, No. 1604145.
- (9) Poudel, B.; Hao, Q.; Ma, Y.; Lan, Y.; Minnich, A.; Yu, B.; Yan, X.; Wang, D.; Muto, A.; Vashaee, D.; Chen, X.; Liu, J.; Dresselhaus, M. S.; Chen, G.; Ren, Z. High-Thermoelectric Performance of Nanostructured Bismuth Antimony Telluride Bulk Alloys. *Science* **2008**, *320*, 634–638.
- (10) Dresselhaus, M. S.; Chen, G.; Tang, M. Y.; Yang, R. G.; Lee, H.; Wang, D. Z.; Ren, Z. F.; Fleurial, J. P.; Gogna, P. New Directions for Low-Dimensional Thermoelectric Materials. *Adv. Mater.* **2007**, *19*, 1043–1053.
- (11) Shuai, J.; Mao, J.; Song, S.; Zhang, Q.; Chen, G.; Ren, Z. Recent Progress and Future Challenges on Thermoelectric Zintl Materials. *Mater. Today Phys.* **2017**, *1*, 74–95.
- (12) Terasaki, I.; Sasago, Y.; Uchinokura, K. Large Thermoelectric Power in NaCo2O4 Single Crystals. *Phys. Rev. B* 1997, 56, No. R12685.
- (13) Li, S.; Funahashi, R.; Matsubara, I.; Ueno, K.; Sodeoka, S.; Yamada, H. Synthesis and Thermoelectric Properties of the New Oxide Materials  $Ca_{3-x}Bi_xCo_4O_{9+\delta}$  (0.0<x<0.75). *Chem. Mater.* **2000**, 12, 2424–2427.
- (14) Shikano, M.; Funahashi, R. Electrical and Thermal Properties of Single-Crystalline  $(Ca_2CoO_3)_{0.7}CoO_2$  with a  $Ca_3Co_4O_9$  Structure. *Appl. Phys. Lett.* **2003**, 82, 1851–1853.
- (15) Singh, D. Quantum Critical Behavior and Possible Triplet Superconductivity in Electron-Doped CoO<sub>2</sub> Sheets. *Phys. Rev. B* **2003**, 68, No. 020503.
- (16) Shizuya, M.; Isobe, M.; Baba, Y.; Nagai, T.; Osada, M.; Kosuda, K.; Takenouchi, S.; Matsui, Y.; Takayama-Muromachi, E. New Misfit-Layered Cobalt Oxide (CaOH)<sub>1.14</sub>CoO<sub>2</sub>. *J. Solid State Chem.* **2007**, 180. 249–259.
- (17) Isobe, M.; Shizuya, M.; Takayama-Muromachi, E. Crystal Structure and Physical Properties of a Misfit-Layered Cobaltite (CaOH)<sub>1.14</sub>CoO<sub>2</sub>. *J. Magn. Magn. Mater.* **2007**, 310, e269–e271.
- (18) Miyazaki, Y.; Onoda, M.; Oku, T.; Kikuchi, M.; Ishii, Y.; Ono, Y.; Morii, Y.; Kajitani, T. Modulated Structure of the Thermoelectric Compound [Ca<sub>2</sub>CoO<sub>3</sub>]<sub>0.62</sub>CoO<sub>2</sub>. *J. Phys. Soc. Jpn.* **2002**, 71, 491–497.
- (19) De Vaulx, C.; Julien, M.-H.; Berthier, C.; Hébert, S.; Pralong, V.; Maignan, A. Electronic Correlations in CoO<sub>2</sub>, the Parent Compound of Triangular Cobaltates. *Phys. Rev. Lett.* **2007**, *98*, No. 246402.
- (20) Matsubara, I.; Funahashi, R.; Shikano, M.; Sasaki, K.; Enomoto, H. Cation Substituted  $(Ca_2CoO_3)_xCoO_2$  Films and Their Thermoelectric Properties. *Appl. Phys. Lett.* **2002**, *80*, 4729–4731.
- (21) Xu, G.; Funahashi, R.; Shikano, M.; Pu, Q.; Liu, B. High Temperature Transport Properties of Ca<sub>3-x</sub>Na<sub>x</sub>Co<sub>4</sub>O<sub>9</sub> System. *Solid State Commun.* **2002**, 124, 73–76.
- (22) Koumoto, K.; Funahashi, R.; Guilmeau, E.; Miyazaki, Y.; Weidenkaff, A.; Wang, Y.; Wan, C. Thermoelectric Ceramics for Energy Harvesting. *J. Am. Ceram. Soc.* **2013**, *96*, 1–23.
- (23) Liu, Y.; Wang, W.; Yang, J.; Li, S. Recent Advances of Layered Thermoelectric Materials. *Adv. Sustainable Syst.* **2018**, 2, No. 1800046.
- (24) Mikami, M.; Chong, K.; Miyazaki, Y.; Kajitani, T.; Inoue, T.; Sodeoka, S.; Funahashi, R. Bi-Substitution Effects on Crystal Structure and Thermoelectric Properties of Ca<sub>3</sub>Co<sub>4</sub>O<sub>9</sub> Single Crystals. *Jpn. J. Appl. Phys.* **2006**, *45*, 4131–4136.
- (25) Boyle, C.; Carvillo, P.; Chen, Y.; Barbero, E. J.; McIntyre, D.; Song, X. Grain Boundary Segregation and Thermoelectric Performance Enhancement of Bismuth Doped Calcium Cobaltite. *J. Eur. Ceram. Soc.* **2016**, *36*, 601–607.

- (26) Fergus, J. W. Oxide Materials for High Temperature Thermoelectric Energy Conversion. *J. Eur. Ceram. Soc.* **2012**, *32*, 525–540.
- (27) Chen, Z.; Ge, B.; Li, W.; Lin, S.; Shen, J.; Chang, Y.; Hanus, R.; Snyder, G. J.; Pei, Y. Vacancy-Induced Dislocations Within Grains for High-Performance PbSe Thermoelectrics. *Nat. Commun.* **2017**, *8*, No. 13828.
- (28) Kim, S. I.; Lee, K. H.; Mun, H. A.; Kim, H. S.; Hwang, S. W.; Roh, J. W.; Yang, D. J.; Shin, W. H.; Li, X. S.; Lee, Y. H.; et al. Dense Dislocation Arrays Embedded in Grain Boundaries for High-Performance Bulk Thermoelectrics. *Science* **2015**, 348, 109–114.
- (29) Kanatzidis, M. G. Nanostructured Thermoelectrics: The New Paradigm? *Chem. Mater.* **2010**, 22, 648–659.
- (30) Sedmidubský, D.; Jakeš, V.; Jankovský, O.; Leitner, J.; Sofer, Z.; Hejtmánek, J. Phase Equilibria in Ca–Co–O System. *J. Solid State Chem.* **2012**, *194*, 199–205.
- (31) Mikami, M.; Funahashi, R.; Yoshimura, M.; Mori, Y.; Sasaki, T. High-Temperature Thermoelectric Properties of Single-Crystal Ca<sub>3</sub>Co<sub>2</sub>O<sub>6</sub>. *J. Appl. Phys.* **2003**, *94*, 6579–6582.
- (32) Lotgering, F. K. Topotactical Reactions with Ferrimagnetic Oxides Having Hexagonal Crystal Structures—I. *J. Inorg. Nucl. Chem.* **1959**, *9*, 113–123.
- (33) Romo-De-La-Cruz, C.; Liang, L.; Navia, S. A. P.; Chen, Y.; Prucz, J.; Song, X. Role of Oversized Dopant Potassium on the Nanostructure and Thermoelectric Performance of Calcium Cobaltite Ceramics. Sustainable Energy Fuels 2018, 2, 876–881.
- (34) Carvillo, P.; Chen, Y.; Boyle, C.; Barnes, P. N.; Song, X. Thermoelectric Performance Enhancement of Calcium Cobaltite through Barium Grain Boundary Segregation. *Inorg. Chem.* **2015**, *54*, 9027–9032.
- (35) Wuensch, B. J.; Vasilos, T. Origin of Grain-Boundary Diffusion in MgO. J. Am. Ceram. Soc. 1966, 49, 433–436.
- (36) Papillon, F.; Rohrer, G. S.; Wynblatt, P. Effect of Segregating Impurities on the Grain-Boundary Character Distribution of Magnesium Oxide. *J. Am. Ceram. Soc.* **2009**, *92*, 3044–3051.
- (37) Rohrer, G. S. Measuring and Interpreting the Structure of Grain-Boundary Networks. J. Am. Ceram. Soc. 2011, 94, 633-646.
- (38) Dake, J. M.; Oddershede, J.; Sørensen, H. O.; Werz, T.; Shatto, J. C.; Uesugi, K.; Schmidt, S.; Krill, C. E. Direct Observation of Grain Rotations During Coarsening of a Semisolid Al—Cu Alloy. *Proc. Natl. Acad. Sci. U.S.A.* **2016**, *113*, E5998—E6006.
- (39) Rajeevan, N.; Kumar, R.; Shukla, D.; Thakur, P.; Brookes, N.; Chae, K.; Choi, W.; Gautam, S.; Arora, S.; Shvets, I.; Pradyumnan, P. P. Bi-Substitution-Induced Magnetic Moment Distribution in Spinel Bi<sub>x</sub>Co<sub>2-x</sub>MnO<sub>4</sub> Multiferroic. *J. Phys.: Condens. Matter* **2009**, 21, No. 406006.
- (40) Curtarolo, S.; Hart, G. L.; Nardelli, M. B.; Mingo, N.; Sanvito, S.; Levy, O. The High-Throughput Highway to Computational Materials Design. *Nat. Mater.* **2013**, *12*, 191–201.
- (41) Tschöpe, A.; Kilassonia, S.; Zapp, B.; Birringer, R. Grain-Size-Dependent Thermopower of Polycrystalline Cerium Oxide. *Solid State Ionics* **2002**, *149*, 261–273.
- (42) Zide, J. M. O.; Vashaee, D.; Bian, Z.; Zeng, G.; Bowers, J.; Shakouri, A.; Gossard, A. Demonstration of Electron Filtering to Increase the Seebeck Coefficient in In<sub>0.53</sub>Ga<sub>0.47</sub>As/In<sub>0.53</sub>Ga<sub>0.28</sub>Al<sub>0.19</sub>As Superlattices. *Phys. Rev. B* **2006**, *74*, No. 205335.
- (43) Yu, Z.; Cantwell, P. R.; Gao, Q.; Yin, D.; Zhang, Y.; Zhou, N.; Rohrer, G. S.; Widom, M.; Luo, J.; Harmer, M. P. Segregation-Induced Ordered Superstructures at General Grain Boundaries in a Nickel-Bismuth Alloy. *Science* **2017**, *358*, 97–101.
- (44) Shibata, N.; Findlay, S.; Azuma, S.; Mizoguchi, T.; Yamamoto, T.; Ikuhara, Y. Atomic-Scale Imaging of Individual Dopant Atoms in a Buried Interface. *Nat. Mater.* **2009**, *8*, 654–658.
- (45) Wang, Z.; Saito, M.; McKenna, K. P.; Gu, L.; Tsukimoto, S.; Shluger, A. L.; Ikuhara, Y. Atom-Resolved Imaging of Ordered Defect Superstructures at Individual Grain Boundaries. *Nature* **2011**, 479, 380–383.
- (46) Song, X.; Daniels, G.; Feldmann, D. M.; Gurevich, A.; Larbalestier, D. Electromagnetic, Atomic Structure and Chemistry

- Changes Induced by Ca-Doping of Low-Angle  $YBa_2Cu_3O_{7-\delta}$  Grain Boundaries. *Nat. Mater.* **2005**, *4*, 470–475.
- (47) Yang, J.; Yip, H. L.; Jen, A. K. Y. Rational Design of Advanced Thermoelectric Materials. *Adv. Energy Mater.* **2013**, *3*, 549–565.
- (48) Ohta, H.; Sugiura, K.; Koumoto, K. Recent Progress in Oxide Thermoelectric Materials: p-type Ca<sub>3</sub>Co<sub>4</sub>O<sub>9</sub> and n-type SrTiO<sub>3</sub>-. *Inorg. Chem.* **2008**, *47*, 8429–8436.
- (49) Hao, Q.; Xu, D.; Lu, N.; Zhao, H. High-Throughput ZT Predictions of Nanoporous Bulk Materials as Next Generation Thermoelectric Materials: A Material Genome Approach. *Phys. Rev.* B **2016**, 93, No. 205206.
- (50) Ma, Y.; Vartak, P. B.; Nagaraj, P.; Wang, R. Y. Thermoelectric Properties of Copper Chalcogenide Alloys Deposited Via the Solution-Phase Using a Thiol—Amine Solvent Mixture. *RSC Adv.* **2016**, *6*, 99905—99913.
- (51) Boyle, C.; Liang, L.; Romo-De-La-Cruz, C.-O.; Johnson, R.; Chen, Y.; Prucz, J.; Cakmak, E.; Watkins, T. R.; Lara-Curzio, E.; Song, X. Improving the Thermoelectric Performance and Thermal Stability of  $\text{Ca}_3\text{Co}_4\text{O}_{9+\delta}$  Ceramics by Sintering in Oxygen Atmosphere. *J. Sol-Gel Sci. Technol.* **2018**, 85, 712–722.
- (52) Joshi, G.; Lee, H.; Lan, Y.; Wang, X.; Zhu, G.; Wang, D.; Gould, R. W.; Cuff, D. C.; Tang, M. Y.; Dresselhaus, M. S.; et al. Enhanced Thermoelectric Figure-of-Merit in Nanostructured p-type Silicon Germanium Bulk Alloys. *Nano Lett.* **2008**, *8*, 4670–4674.
- (53) Biswas, K.; He, J.; Blum, I. D.; Wu, C.-I.; Hogan, T. P.; Seidman, D. N.; Dravid, V. P.; Kanatzidis, M. G. High-Performance Bulk Thermoelectrics with All-Scale Hierarchical Architectures. *Nature* **2012**, 489, 414–418.
- (54) Hong, M.; Chen, Z. G.; Yang, L.; Zou, Y. C.; Dargusch, M. S.; Wang, H.; Zou, J. Realizing ZT of 2.3 in  $Ge_{1-x-y}Sb_xIn_yTe$  via Reducing the Phase-Transition Temperature and Introducing Resonant Energy Doping. *Adv. Mater.* **2018**, *30*, No. 1705942.
- (55) LeBlanc, S.; Yee, S. K.; Scullin, M. L.; Dames, C.; Goodson, K. E. Material and Manufacturing Cost Considerations for Thermoelectrics. *Renewable Sustainable Energy Rev.* **2014**, *32*, 313–327.
- (56) He, J.; Liu, Y.; Funahashi, R. Oxide Thermoelectrics: The Challenges, Progress, and Outlook. *J. Mater. Res.* **2011**, 26, No. 1762. (57) Song, X.; Paredes Navia, S. A.; Liang, L.; Boyle, C.; Romo-De-La-Cruz, C.-O.; Jackson, B.; Hinerman, A.; Wilt, M.; Prucz, J.; Chen, Y. Grain Boundary Phase Segregation for Dramatic Improvement of the Thermoelectric Performance of Oxide Ceramics. *ACS Appl. Mater. Interfaces* **2018**, *10*, 39018–39024.
- (58) Duan, C.; Tong, J.; Shang, M.; Nikodemski, S.; Sanders, M.; Ricote, S.; Almansoori, A.; O'Hayre, R. Readily Processed Protonic Ceramic Fuel Cells with High Performance at Low Temperatures. *Science* **2015**, 349, 1321–1326.
- (59) Wang, D.; Chen, L.; Wang, Q.; Li, J. Fabrication and Thermoelectric Properties of  $Ca_{3-x}Dy_xCo_4O_{9+\delta}$  System. J. Alloys Compd. **2004**, 376, 58–61.
- (60) Liu, H. Q.; Zhao, X. B.; Liu, F.; Song, Y.; Sun, Q.; Zhu, T. J.; Wang, F. P. Effect of Gd-doping on Thermoelectric Properties of  $Ca_3Co_4O_{9+\delta}$  Ceramics. *J. Mater. Sci.* **2008**, *43*, 6933–6937.
- (61) Wang, Y.; Sui, Y.; Cheng, J.; Wang, X.; Su, W. Comparison of the High Temperature Thermoelectric Properties for Ag-Doped and Ag-Added  $Ca_3Co_4O_9$ . *J. Alloys Compd.* **2009**, 477, 817–821.
- (62) Xu, L.; Li, F.; Wang, Y. High-Temperature Transport and Thermoelectric Properties of Ca<sub>3</sub>Co<sub>4-x</sub>Ti<sub>x</sub>O<sub>9</sub>. *J. Alloys Compd.* **2010**, 501, 115–119.
- (63) Van Nong, N.; Pryds, N.; Linderoth, S.; Ohtaki, M. Enhancement of the Thermoelectric Performance of p-Type Layered Oxide  $Ca_3Co_4O_{9+\delta}$  Through Heavy Doping and Metallic Nanoinclusions. *Adv. Mater.* **2011**, 23, 2484–2490.
- (64) Tian, R.; Zhang, T.; Chu, D.; Donelson, R.; Tao, L.; Li, S. Enhancement of High Temperature Thermoelectric Performance in Bi, Fe Co-Doped Layered Oxide-Based Material  $Ca_3Co_4O_{9+\delta}$ . J. Alloys Compd. **2014**, 615, 311–315.
- (65) Bittner, M.; Helmich, L.; Nietschke, F.; Geppert, B.; Oeckler, O.; Feldhoff, A. Porous  $Ca_3Co_4O_9$  with Enhanced Thermoelectric

- Properties Derived from Sol-Gel Synthesis. J. Eur. Ceram. Soc. 2017, 37, 3909–3915.
- (66) Bittner, M.; Kanas, N.; Hinterding, R.; Steinbach, F.; Groeneveld, D.; Wemhoff, P.; Wiik, K.; Einarsrud, M.-A.; Feldhoff, A. Triple-Phase Ceramic 2D Nanocomposite with Enhanced Thermoelectric Properties. *J. Eur. Ceram. Soc.* **2019**, 39, 1237–1244. (67) Xu, G.; Funahashi, R.; Shikano, M.; Matsubara, I.; Zhou, Y. Thermoelectric Properties of the Bi- and Na-Substituted Ca<sub>3</sub>Co<sub>4</sub>O<sub>9</sub> System. *Appl. Phys. Lett.* **2002**, 80, 3760–3762.
- (68) Wang, D.; Chen, L.; Yao, Q.; Li, J. High-Temperature Thermoelectric Properties of  $Ca_3Co_4O_{9+\delta}$  with Eu Substitution. *Solid State Commun.* **2004**, *129*, 615–618.
- (69) Mikami, M.; Ando, N.; Funahashi, R. The Effect of Ag Addition on Electrical Properties of the Thermoelectric Compound Ca<sub>3</sub>Co<sub>4</sub>O<sub>9</sub>. *J. Solid State Chem.* **2005**, *178*, 2186–2190.
- (70) Wang, Y.; Sui, Y.; Cheng, J.; Wang, X.; Miao, J.; Liu, Z.; Qian, Z.; Su, W. High Temperature Transport and Thermoelectric Properties of Ag-Substituted  $Ca_3Co_4O_{9+\delta}$  System. J. Alloys Compd. **2008**, 448, 1–5.
- (71) Liu, H. Q.; Song, Y.; Zhang, S. N.; Zhao, X. B.; Wang, F. P. Thermoelectric Properties of  $Ca_{3-x}Y_xCo_4O_{9+\delta}$  Ceramics. *J. Phys. Chem. Solids* **2009**, 70, 600–603.
- (72) Wang, Y.; Sui, Y.; Wang, X.; Su, W.; Liu, X. Enhanced High Temperature Thermoelectric Characteristics of Transition Metals Doped Ca<sub>3</sub>Co<sub>4</sub>O<sub>9+6</sub> by Cold High-Pressure Fabrication. *J. Appl. Phys.* **2010**, *107*, No. 033708.
- (73) Nong, N. V.; Liu, C. J.; Ohtaki, M. Improvement on the High Temperature Thermoelectric Performance of Ga-Doped Misfit-Layered  $Ca_3Co_{4-x}Ga_xO_{9+\delta}$  (x = 0, 0.05, 0.1, and 0.2). *J. Alloys Compd.* **2010**, 491, 53–56.
- (74) Zhang, F. P.; Zhang, X.; Lu, Q. M.; Zhang, J. X.; Liu, Y. Q.; Zhang, G. Z. Preparation and High Temperature Thermoelectric Properties of  $Ca_{3-x}Ag_xCo_4O_{9+\delta}$  Oxides. *Solid State Ionics* **2011**, 201, 1–5.
- (75) Pei, J.; Chen, G.; Zhou, N.; Lu, D. Q.; Xiao, F. High Temperature Transport and Thermoelectric Properties of  $Ca_{3-x}Er_xCo_4O_{9+\delta}$ . Phys. B **2011**, 406, 571–574.
- (76) Nong, N. V.; Liu, C.-J.; Ohtaki, M. High-Temperature Thermoelectric Properties of Late Rare Earth-Doped Ca<sub>3</sub>Co<sub>4</sub>O<sub>9+δ</sub>. *J. Alloys Compd.* **2011**, 509, 977–981.
- (77) Zhang, F. P.; Zhang, X.; Lu, Q. M.; Zhang, J. X.; Liu, Y. Q.; Zhang, G. Z. Effects of Pr Doping on Thermoelectric Transport Properties of Ca<sub>3-x</sub>Pr<sub>x</sub>Co<sub>4</sub>O<sub>9</sub>. *Solid State Sci.* **2011**, *13*, 1443–1447.
- (78) Prasoetsopha, N.; Pinitsoontorn, S.; Kamwanna, T.; Amornkitbamrung, V.; Kurosaki, K.; Ohishi, Y.; Muta, H.; Yamanaka, S. The Effect of Cr Substitution on the Structure and Properties of Misfit-Layered Ca<sub>3</sub>Co<sub>4-x</sub>Cr<sub>x</sub>O<sub>9+δ</sub> Thermoelectric Oxides. *J. Alloys Compd.* **2014**, 588, 199–205.
- (79) Butt, S.; Liu, Y.-C.; Lan, J.-L.; Shehzad, K.; Zhan, B.; Lin, Y.; Nan, C.-W. High-Temperature Thermoelectric Properties of La and Fe Co-Doped Ca—Co—O Misfit-Layered Cobaltites Consolidated by Spark Plasma Sintering. *J. Alloys Compd.* **2014**, *588*, 277—283.
- (80) Butt, S.; Xu, W.; He, W. Q.; Tan, Q.; Ren, G. K.; Lin, Y.; Nan, C.-W. Enhancement of Thermoelectric Performance in Cd-Doped Ca<sub>3</sub>Co<sub>4</sub>O<sub>9</sub> via Spin Entropy, Defect Chemistry and Phonon Scattering. *J. Mater. Chem. A* **2014**, *2*, 19479–19487.
- (81) Gunes, M.; Ozenbas, M. Effect of Grain Size and Porosity on Phonon Scattering Enhancement of Ca<sub>3</sub>Co<sub>4</sub>O<sub>9</sub>. *J. Alloys Compd.* **2015**, 626, 360–367.
- (82) Huang, C. S.; Zhang, F. P.; Zhang, X.; Lu, Q. M.; Zhang, J. X.; Liu, Z. Y. Enhanced Thermoelectric Figure of Merit Through Electrical and Thermal Transport Modulation by Dual-Doping and Texture Modulating for  $Ca_3Co_4O_{9+\delta}$  Oxide Materials. *J. Alloys Compd.* **2016**, *687*, 87–94.
- (83) Sotelo, A.; Costa, F. M.; Ferreira, N. M.; Kovalevsky, A.; Ferro, M. C.; Amaral, V. S.; Amaral, J. S.; Rasekh, S.; Torres, M. A.; Madre, M. A.; Diez, J. C. Tailoring Ca<sub>3</sub>Co<sub>4</sub>O<sub>9</sub> Microstructure and Performances Using a Transient Liquid Phase Sintering Additive. *J. Eur. Ceram. Soc.* **2016**, *36*, 1025–1032.

- (84) Presečnik, M.; de Boor, J.; Bernik, S. Synthesis of Single-Phase Ca<sub>3</sub>Co<sub>4</sub>O<sub>9</sub> Ceramics and Their Processing for a Microstructure-Enhanced Thermoelectric Performance. *Ceram. Int.* **2016**, 42, 7315–7327
- (85) Porokhin, S.; Shvanskaya, L.; Khovaylo, V.; Vasiliev, A. Effect of NaF Doping on the Thermoelectric Properties of Ca<sub>3</sub>Co<sub>4</sub>O<sub>9</sub>. *J. Alloys Compd.* **2017**, *695*, 2844–2849.
- (86) Boyle, C.; Liang, L.; Chen, Y.; Prucz, J.; Cakmak, E.; Watkins, T. R.; Lara-Curzio, E.; Song, X. Competing Dopants Grain Boundary Segregation and Resultant Seebeck Coefficient and Power Factor Enhancement of Thermoelectric Calcium Cobaltite Ceramics. *Ceram. Int.* **2017**, 43, 11523–11528.
- (87) Hira, U.; Han, L.; Norrman, K.; Christensen, D. V.; Pryds, N.; Sher, F. High-Temperature Thermoelectric Properties of Na- and W-Doped Ca<sub>3</sub>Co<sub>4</sub>O<sub>9</sub> System. *RSC Adv.* **2018**, *8*, 12211–12221.
- (88) Torres, M. A.; Costa, F. M.; Flahaut, D.; Touati, K.; Rasekh, S.; Ferreira, N. M.; Allouche, J.; Depriester, M.; Madre, M. A.; Kovalevsky, A. V.; Diez, J. C.; Sotelo, A. Significant Enhancement of the Thermoelectric Performance in Ca<sub>3</sub>Co<sub>4</sub>O<sub>9</sub> Thermoelectric Materials Through Combined Strontium Substitution and Hot-Pressing Process. *J. Eur. Ceram. Soc.* **2019**, 39, 1186–1192.
- (89) Bittner, M.; Kanas, N.; Hinterding, R.; Steinbach, F.; Räthel, J.; Schrade, M.; Wiik, K.; Einarsrud, M.-A.; Feldhoff, A. A Comprehensive Study on Improved Power Materials for High-Temperature Thermoelectric Generators. *J. Power Sources* **2019**, *410–411*, 143–151.